HAL open science

Balance control using both ZMP and COM height variations: A convex boundedness approach

Stéphane Caron, Bastien Mallein

To cite this version:

Stéphane Caron, Bastien Mallein. Balance control using both ZMP and COM height variations: A convex boundedness approach. 2017. hal-01590509v1

HAL Id: hal-01590509

https://hal.science/hal-01590509v1

Preprint submitted on 19 Sep 2017 (v1), last revised 26 Feb 2018 (v4)

HAL is a multi-disciplinary open access archive for the deposit and dissemination of scientific research documents, whether they are published or not. The documents may come from teaching and research institutions in France or abroad, or from public or private research centers.

L'archive ouverte pluridisciplinaire **HAL**, est destinée au dépôt et à la diffusion de documents scientifiques de niveau recherche, publiés ou non, émanant des établissements d'enseignement et de recherche français ou étrangers, des laboratoires publics ou privés.

Distributed under a Creative Commons Attribution - ShareAlike 4.0 International License

Balance control using both ZMP and COM height variations: A convex boundedness approach

Stéphane Caron and Bastien Mallein

***Abstract*— Developments for 3D control of the center of mass (CoM) are currently located in two local minima: on the one hand, methods that allow CoM height variations but only work in the 2D sagittal plane; on the other hand, nonconvex centroidal models that are delicate to handle. This paper presents an alternative that controls the CoM in 3D by predictive control over a *convex* optimization problem. The key to this development is the notion of boundedness condition, which quantifies convexly the viability of CoM trajectories.**

I. Introduction

Three-dimensional control of the center of mass (CoM) follows in the wake of major achievements obtained in 2D locomotion with the linear inverted pendulum mode (LIPM) [1]. The core idea of the LIPM was to keep the CoM in a plane, which made the model tractable and paved the way for key discoveries, including (but not restricted to) the capture point [2] and capture-point based feedback control [3], subsequently applied to successful walking controllers [4], [5].

For a while, the ability to leverage vertical CoM motions seemed lost on the way, but recent developments showed a regain of interest for this capacity [6], [7], [8]. All of them share a design choice that can be traced back to the seminal work of Pratt and Drakunov [9]: they interpolate CoM trajectories in a 2D sagittal plane for the inverted pendulum model (IPM) with fixed center of pressure (CoP). The key result of [9] is the conservation of the "orbital energy" of a CoM path, a variational principle that was later translated into a predictive controller in an equally inspirational study by Koolen *et al.* [7]. Ramos and Hauser [6] also noticed that the capture point, interpreted as *point where to step*, was a function of the CoM path, which they computed via a single shooting method. Interestingly, Hopkins *et al.* pointed out that vertical CoM motions amount to turn the constant ω of the LIPM into a time-varying function $\omega(t)$ [10]. They brought to light a differential equation that this function must satisfy, and used it to compute back $\omega(t)$ from, once again, an *a priori* CoM-height trajectory.

Different as they may seem, the variational and point-where-to-step approaches are two instances of the same underlying concept: convergence of the system towards a steady state requires that its divergent component of motion stays bounded. Lanari *et al.* [11] showed how the condition for this to happen involves an integral over the future trajectory of the system (one can see a similar integral in the orbital energy), which they named the *boundedness condition*.

In what follows, we break from existing approaches by working on $\omega(t)$ *per se* rather than as a result of CoM trajectories. This is made possible by the derivation of the boundedness condition for the 3D IPM (Section II), which is then cast into a convex optimization problem for 2D and 3D control of the CoM (Sections III and IV). The resulting predictive controller is implemented and tested in Section V.

II. Boundedness condition of the IPM

The equation of motion of the inverted pendulum model is:

$$\ddot{\boldsymbol{c}}(t) = \lambda(t)(\boldsymbol{c}(t) - \boldsymbol{r}(t)) + \boldsymbol{g} \tag{1}$$

where $\boldsymbol{c}$ is the center of mass of the robot, $\boldsymbol{r}$ is the center of pressure under its contacting foot, and $\boldsymbol{g} = -g\boldsymbol{e}_z$ is the gravity vector. This model evolves under the feasibility conditions that $\lambda \geq 0$ (unilaterality of contact) and that the CoP $\boldsymbol{r}$ belongs to the contact area.

To alleviate calculations, let us formulate the divergent component of motion [5] of this model as a velocity rather than a point:

$$\boldsymbol{\xi}(t) = \dot{\boldsymbol{c}}(t) - \dot{\boldsymbol{r}}(t) + \omega(t)(\boldsymbol{c}(t) - \boldsymbol{r}(t)) \tag{2}$$

where $\omega(t)$ is a solution to the differential equation [10]:

$$\dot{\omega} = \omega^2 - \lambda \tag{3}$$

The interest of this choice appears when differentiating the divergent component of motion:

$$\dot{\boldsymbol{\xi}} = (\lambda + \dot{\omega})(\boldsymbol{c} - \boldsymbol{r}) + \boldsymbol{g} - \ddot{\boldsymbol{r}} = \omega\boldsymbol{\xi} + \boldsymbol{g} - \ddot{\boldsymbol{r}} \tag{4}$$

The solution to this first-order differential equation is:

$$\boldsymbol{\xi}(t) = \left(\boldsymbol{\xi}(0) + \int_0^t e^{-\Omega(\tau)}(\boldsymbol{g} - \ddot{\boldsymbol{r}}(\tau))\mathrm{d}\tau\right) e^{\Omega(t)} \tag{5}$$

where Ω is the primitive of ω such that $\Omega(0) = 0$. In the LIPM where ω is a constant, $\Omega(t) = \omega t$ and this equation is equivalent to the well-known capture point dynamics.

To be viable [12], the trajectory of the system must be bounded, which implies that the above expression does not diverge despite its exponential factor. This necessary condition for viability is known as the *boundedness condition* [11], and is written here:

$$\int_0^\infty (\ddot{\boldsymbol{r}}(t) - \boldsymbol{g})e^{-\Omega(t)}\mathrm{d}t = \boldsymbol{\xi}(0) \tag{6}$$

This work is supported in part by the H2020 EU project COMANOID `http://www.comanoid.eu/`, RIA No 645097.

S. Caron is with the Montpellier Laboratory of Informatics, Robotics and Microelectronics (LIRMM), CNRS–University of Montpellier, 860 rue de St-Priest, 34095 Montpellier, France.

B. Mallein is with the Laboratoire Analyse, Géométrie et Applications (LAGA), CNRS–Paris 13 University, 99 avenue Jean-Baptiste Clément, 93430 Villetaneuse, France.

Corresponding author: `stephane.caron@normalesup.org`

Note how this requirement involves both the CoP trajectory $\boldsymbol{r}(t)$ and leg-stiffness trajectory $\lambda(t)$: the former is integrated through $\ddot{\boldsymbol{r}}(t)$, while the latter is embedded in $\Omega(t)$.

A. Decoupling of the boundedness constraint

Let us express all coordinates in the inertial frame depicted in Figure 1. In what follows, we will use the subscript i ("initial") to indicate values at $t = 0$, and f ("final") for stationary values obtained as $t \to \infty$. The origin of the inertial frame is taken at the stationary CoP position $\boldsymbol{r}_f = \boldsymbol{0}$ where we want the robot to stop. (The stationary CoM position is then $\boldsymbol{c}_f = \ell \boldsymbol{e}_z$ for a desired leg length ℓ.) The two vectors $\boldsymbol{e}_x$ and $\boldsymbol{e}_y$ are horizontal, and $\boldsymbol{e}_x$ is chosen aligned with the horizontal projection of $\boldsymbol{r}_f - \boldsymbol{c}_i$. Note that, despite being defined from the initial state of the system, the frame is *inertial*.

The CoP $\boldsymbol{r}$ is feasible if and only if it lies on the contact surface. Denoting by $\boldsymbol{n}$ the contact normal, this means that $\boldsymbol{r} \cdot \boldsymbol{n} = 0$, or equivalently that $\boldsymbol{r}$ can be written as a combination $\boldsymbol{r} = \alpha \boldsymbol{t} + \beta \boldsymbol{b}$ of two vectors (not necessarily orthogonal) belonging to the contact surface. We choose:

$$\boldsymbol{t} = \cos\phi \boldsymbol{e}_x + \sin\phi \boldsymbol{e}_z \qquad \boldsymbol{b} = \cos\theta \boldsymbol{e}_y + \sin\theta \boldsymbol{e}_z \tag{7}$$

where $(\boldsymbol{t} \cdot \boldsymbol{n}) = 0$ implies that $\phi = \arctan(-(\boldsymbol{e}_x \cdot \boldsymbol{n})/(\boldsymbol{e}_z \cdot \boldsymbol{n}))$, and similarly for θ. The coordinates of $\boldsymbol{r}$ in the inertial frame become:

$$\begin{bmatrix} r_x(t) \\ r_y(t) \\ r_z(t) \end{bmatrix} = \begin{bmatrix} \alpha(t)\cos\phi \\ \beta(t)\cos\theta \\ \alpha(t)\sin\phi + \beta(t)\sin\theta \end{bmatrix} \tag{8}$$

With these notations, the boundedness condition (6) is:

$$\xi_x(0) = \int_0^\infty \ddot{\alpha}(t)\cos\phi\, e^{-\Omega(t)} \mathrm{d}t \tag{9}$$

$$\xi_y(0) = \int_0^\infty \ddot{\beta}(t)\cos\theta\, e^{-\Omega(t)} \mathrm{d}t \tag{10}$$

$$\xi_z(0) = \int_0^\infty \left[g + \ddot{\alpha}(t)\sin\phi + \ddot{\beta}(t)\sin\theta \right] e^{-\Omega(t)} \mathrm{d}t \tag{11}$$

By linear combination of these three expressions, condition (11) can be rewritten as:

$$\int_0^\infty e^{-\Omega(t)} \mathrm{d}t = \frac{\dot{\bar{z}}_i + \omega_i \bar{z}_i}{g} \tag{12}$$

where $\bar{z} = z - x\tan\phi - y\tan\theta = (\boldsymbol{c} \cdot \boldsymbol{n})/(\boldsymbol{e}_z \cdot \boldsymbol{n})$. Next, recall from Equation (2) that:

$$\xi_x(0) = \dot{x}_i + \omega_i x_i - (\dot{r}_{x,i} + \omega_i r_{x,i}) \tag{13}$$

Integrating by parts Equation (9) twice yields:

$$\int_0^\infty \ddot{r}_x(t) e^{-\Omega(t)} \mathrm{d}t = \int_0^\infty r_x(t)\lambda(t) e^{-\Omega(t)} \mathrm{d}t - (\dot{r}_{x,i} + \omega_i r_{x,i})$$

Now, combine these two equations to get:

$$\int_0^\infty r_x(t)\lambda(t) e^{-\Omega(t)} \mathrm{d}t = \dot{x}_i + \omega_i x_i \tag{14}$$

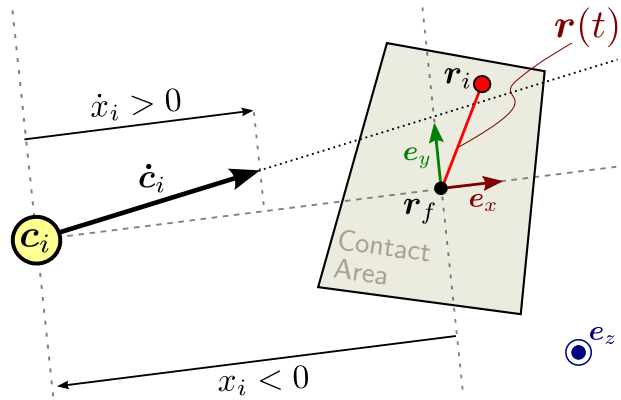

Fig. 1. **Definition of the inertial frame** $(\boldsymbol{e}_x, \boldsymbol{e}_y, \boldsymbol{e}_z)$**.** The frame is rooted at the stationary CoP location $\boldsymbol{r}_f$. The instantaneous CoM location is denoted by $\boldsymbol{c}_i$. Both vectors $\boldsymbol{e}_x$ and $\boldsymbol{e}_y$ lie in the horizontal plane, and $\boldsymbol{e}_x$ is aligned with the (horizontal projection of the) desired direction of motion $\boldsymbol{r}_f - \boldsymbol{c}_i$.

Applying the same steps from Equation (10) leads to a similar equation of r_y. In summary, we have reformulated the boundedness condition as:

Temporal Boundedness Condition

$$\int_0^\infty e^{-\Omega(t)} \mathrm{d}t = \frac{\dot{\bar{z}}_i + \omega_i \bar{z}_i}{g} \tag{15}$$

$$\int_0^\infty \boldsymbol{p}(t)\lambda(t) e^{-\Omega(t)} \mathrm{d}t = \dot{\bar{\boldsymbol{c}}}_i + \omega_i \bar{\boldsymbol{c}}_i \tag{16}$$

where $\boldsymbol{p}(t) = \begin{bmatrix} r_x(t) & r_y(t) \end{bmatrix}$ and $\bar{\boldsymbol{c}}_i = \begin{bmatrix} x_i & y_i \end{bmatrix}$ are the horizontal projections of the CoP and CoM, respectively.

In the familiar setting of the LIPM, the first equation boils down to:

$$\int_0^\infty e^{-\omega t} \mathrm{d}t = \frac{1}{\omega} = \frac{0 + \omega z}{g} \iff \omega = \sqrt{\frac{g}{z}} \tag{17}$$

Meanwhile, taking $\boldsymbol{p} = 0$ in the second one implies that the traditional LIPM capture point is located at $\boldsymbol{r}_f$. This observation illustrates how the boundedness condition (15)–(16) encompasses the well-known model.

B. Change of variable

Define the adimensional quantity $s(t) = e^{-\Omega(t)}$. This variable ranges from 1 when $t = 0$ to 0 as $t \to \infty$, and its time derivatives are:

$$\dot{s}(t) = -\omega(t)s(t) \tag{18}$$

$$\ddot{s}(t) = \lambda(t)s(t) \tag{19}$$

Thanks to the bijective mapping between s and t, we can characterize ω and λ indistinctly as functions of s or t. Let us choose the former, and denote by $(\cdot)'$ derivatives with respect to s. For instance, $\omega(t) = \omega(s(t))$ and $\dot{\omega} = \dot{s}\omega'$. From Equation (18), this means that $\dot{\omega} = -s\omega\omega'$. Then,

$$\mathrm{d}t = \frac{\mathrm{d}s}{\dot{s}} = -\frac{\mathrm{d}s}{\omega(s)s} \tag{20}$$

$$\lambda = \omega^2 - \dot{\omega} = \omega(\omega + s\omega') = \omega(s\omega)' \tag{21}$$

Applying this change of variable, the boundedness condition (15)–(16) becomes:

Timeless Boundedness Condition

$$\int_0^1 \frac{1}{\omega(s)}\mathrm{d}s = \frac{\dot{\bar{z}}_i + \omega_i \bar{z}_i}{g} \tag{22}$$

$$\int_0^1 \boldsymbol{p}(s)(s\omega)'\mathrm{d}s = \dot{\bar{\boldsymbol{c}}}_i + \omega_i \bar{\boldsymbol{c}}_i \tag{23}$$

Solutions to the boundedness condition (22)–(23) are given by the CoP coordinates and leg stiffness functions $(\omega, \boldsymbol{p})$, which characterize trajectories of the inverted pendulum.

III. Sagittal 2D Balance with Fixed CoP

Let us consider first the case of 2D stabilization in the plane $(\boldsymbol{e}_x, \boldsymbol{e}_z)$ with fixed CoP. Since $r_x = 0$, the boundedness condition becomes:

$$\omega_i = -\frac{\dot{x}_i}{/} x_i \tag{24}$$

$$\dot{z}_i + \omega_i z_i = g \int_0^1 \frac{1}{\omega(s)}\mathrm{d}s \tag{25}$$

Equations (24) implies via (5) that $\dot{x} = -\omega x$, which integrates to $x(t) = x_i e^{-\Omega(t)} = x_i s(t)$: in 2D balance control, the coordinates x and s are proportional. Interpolation over x [7], [9] is therefore equivalent to interpolation over s, and one can recognize in (25) the same principle as the conservation of orbital energy [9]. The benefit of using s rather than x will appear when we move to 3D control.

A. Viability condition

The viability condition $z_{\text{crit}} \geq 0$ derived in [7] for $\lambda \geq 0$ can be seen as a consequence of (25). Indeed, the lower-bounding profile $\underline{\lambda} = 0$ corresponds to $(s\underline{\omega})' = 0$, that is to say, $s\underline{\omega} = \omega_i$. It follows that:

$$\int_0^1 \frac{\mathrm{d}s}{\omega(s)} \geq \int_0^1 \frac{\mathrm{d}s}{\underline{\omega}(s)} = \int_0^1 \frac{s}{\omega_i}\mathrm{d}s = \frac{1}{2\omega_i} \tag{26}$$

$$z_{\text{crit}} = z_i + \frac{\dot{z}_i}{\omega_i} - \frac{g}{2\omega_i^2} = \frac{g}{\omega_i}\left[\int_0^1 \frac{\mathrm{d}s}{\omega(s)} - \frac{1}{2\omega_i}\right] \geq 0 \tag{27}$$

In practice, biped robots cannot exert arbitrary large contact forces, and tend to break contact when ground pressure becomes too low. To reflect this, we will thereafter consider the stricter feasibility condition $\lambda \in [\lambda_{\min}, \lambda_{\max}]$. The corresponding viability condition can be derived in a similar fashion by considering lower- and upper-bounding profiles:

$$\dot{z}_i + \omega_i z_i \leq \frac{g}{\lambda_{\max}}\left[\omega_i + \sqrt{\frac{\lambda_{\max} - \lambda_{\min}}{\lambda_{\min}}}\sqrt{\lambda_{\max} - \omega_i^2}\right] \tag{28}$$

$$\dot{z}_i + \omega_i z_i \geq \frac{g}{\lambda_{\min}}\left[\omega_i - \sqrt{\frac{\lambda_{\max} - \lambda_{\min}}{\lambda_{\max}}}\sqrt{\omega_i^2 - \lambda_{\min}}\right] \tag{29}$$

B. Computing feasible ω solutions

Let us discretize the interval $[0, 1]$ into N fixed segments $0 = s_0 < s_1 < \ldots < s_{N-1} < s_N = 1$, for instance $s_j = i/N$. We compute solutions to the boundedness condition where $\lambda(s)$ is piecewise constant over this subdivision, that is, $\forall s \in [s_j, s_{j+1}], \lambda(s) = \lambda_j$. Define:

$$\Phi(s) \stackrel{\text{def}}{=} s^2\omega^2 \qquad \Delta_j \stackrel{\text{def}}{=} s_{j+1}^2 - s_j^2 \tag{30}$$

Remarking that $\Phi' = 2s\lambda$ from Equation (21), we can directly compute $\Phi(s)$ for $s \in [s_j, s_{j+1}]$ as:

$$\Phi(s) = \sum_{k=0}^{j-1} \lambda_k \Delta_k + \lambda_j(s^2 - s_j^2) \tag{31}$$

In what follows, we use the shorthand $\Phi_j = \Phi(s_j)$.

We can now calculate the right-hand side of the boundedness condition (25):

$$\int_0^1 \frac{\mathrm{d}s}{\omega(s)} = \sum_{j=0}^{N-1} \int_{s_j}^{s_{j+1}} \frac{s\mathrm{d}s}{\sqrt{\Phi_j + \lambda_j(s^2 - s_j^2)}} \tag{32}$$

$$= \sum_{j=0}^{N-1} \int_0^{\Delta_j} \frac{\mathrm{d}v}{2\sqrt{\Phi_j + \lambda_j v}} \tag{33}$$

$$= \sum_{j=0}^{N-1} \frac{1}{\lambda_j}\left[\sqrt{\Phi_j + \lambda_j\Delta_j} - \sqrt{\Phi_j}\right] \tag{34}$$

$$= \sum_{j=0}^{N-1} \frac{\Delta_j}{\sqrt{\Phi_{j+1}} + \sqrt{\Phi_j}} \tag{35}$$

The latter expression is *convex* in the variables $\Phi_1, \ldots, \Phi_N$ (note that $\Phi_0 = 0$), as shown in Appendix A.

Besides boundedness, solutions should enforce three conditions:

- *Feasibility:* $\lambda_{\min} \leq \lambda \leq \lambda_{\max}$, expressed linearly in terms of Φ as $\Delta_j\lambda_{\min} \leq \Phi_{j+1} - \Phi_j \leq \Delta_j\lambda_{\max}$;
- *Initial state:* ω should be equal to ω_i at the initial index $s = 1$, that is to say, $\Phi_N = \omega_i^2$;
- *Stationary state:* a stationary COM height z_f can also be specified via $\Phi_1 = \Delta_0 g/z_f$, or similarly a range of heights $z_{\min} \leq z_f \leq z_{\max}$ used to approximate kinematic reachability.

Wrapping all four conditions together and adding a regularizing cost function over variations of λ, we obtain Convex Problem 1. This problem is "almost" a quadratic program: it has a quadratic cost function and linear constraints, except for Equation (38) which is a convex equality constraint.

C. Model predictive control for 2D balance

Solving Convex Problem 1 can be done fast enough for the control loop, on the scale of 1–3 ms using a general-purpose nonconvex solver (see Section V for a precise statement). At each control cycle, we compute the optimum $\Phi_1^*, \ldots, \Phi_N^*$ of Convex Problem 1 and extract its initial leg stiffness via:

$$\lambda_i^* = \frac{\omega_i^2 - \Phi_{N-1}^*}{\Delta_{N-1}} \tag{36}$$

Convex Problem 1 2D Balance Control

$$\underset{\Phi_1,\ldots,\Phi_N}{\text{minimize}} \sum_{j=1}^{N-1} \left[\frac{\Phi_{j+1}-\Phi_j}{\Delta_j} - \frac{\Phi_j-\Phi_{j-1}}{\Delta_{j-1}}\right]^2 \tag{37}$$

$$\text{subject to} \sum_{j=0}^{N-1} \frac{\Delta_j}{\sqrt{\Phi_{j+1}}+\sqrt{\Phi_j}} = \frac{\dot{\bar{z}}_i + \omega_i \bar{z}_i}{g} \tag{38}$$

$$\Phi_N = \omega_i^2 \tag{39}$$

$$\forall j,\ \lambda_{\min}\Delta_j \leq \Phi_{j+1}-\Phi_j \leq \lambda_{\max}\Delta_j \tag{40}$$

$$\Phi_1 = \Delta_0 g / z_f \tag{41}$$

Convex Problem 2 3D Balance Control

$$\underset{\Phi_1,\ldots,\Phi_N}{\text{minimize}} \sum_{j=1}^{N-1} \left[\frac{\Phi_{j+1}-\Phi_j}{\Delta_j} - \frac{\Phi_j-\Phi_{j-1}}{\Delta_{j-1}}\right]^2 \tag{37}$$

$$\text{subject to} \sum_{j=0}^{N-1} \frac{\Delta_j}{\sqrt{\Phi_{j+1}}+\sqrt{\Phi_j}} - \frac{\bar{z}_i}{g}\sqrt{\Phi_N} = \frac{\dot{\bar{z}}_i}{g} \tag{47}$$

$$\omega_{i,\min}^2 \leq \Phi_N \leq \omega_{i,\max}^2 \tag{48}$$

$$\forall j,\ \lambda_{\min}\Delta_j \leq \Phi_{j+1}-\Phi_j \leq \lambda_{\max}\Delta_j \tag{40}$$

$$\Phi_1 = \Delta_0 g / z_f \tag{41}$$

This value is then sent as reference to the lower-level leg and attitude controllers until the next control cycle. In the standard model-predictive fashion, the rest of the optimal trajectory is discarded. As a matter of fact, the trajectories $\omega(s)$ and $\lambda(s)$ are never explicitly computed, let alone their time counterparts. The operation is possible (see Appendix B) but not necessary for control. Compared to the controller from [7], this solution enforces feasibility constraints $\lambda_{\min} \leq \lambda \leq \lambda_{\max}$ *a priori*, as opposed to an *a posteriori* clipping that may cause free-falling phases in the output trajectory. This comes at the higher cost of convex optimization, versus a single matrix inversion.

IV. 3D Balance

The interest of expressing the boundedness condition in terms of the variable s goes beyond sagittal 2D balance: it also puts the problem in a form that is easier to manipulate mathematically. In 3D balance where the initial velocity $\dot{\boldsymbol{c}}_i$ is not necessarily coplanar with the stationary state, the equality constraint (24) vanishes, replaced by a general condition over CoP trajectories:

$$\int_0^1 \boldsymbol{p}(s)(s\omega)' \mathrm{d}s = \dot{\bar{\boldsymbol{c}}}_i + \omega_i \bar{\boldsymbol{c}}_i \tag{42}$$

Subject to the feasibility conditions:

$$\mathbf{A}\boldsymbol{p} \leq \boldsymbol{b} \tag{43}$$

where the matrix $\mathbf{A}$ and vector $\boldsymbol{b}$ form the halfspace-representation of the contact polygon, which is readily computed from contact geometry. For example, a rectangular contact $|(\boldsymbol{p}\cdot\boldsymbol{e}_w)| \leq W$, $|(\boldsymbol{p}\cdot\boldsymbol{e}_h)| \leq H$ has four inequalities:

$$\pm \begin{bmatrix} \frac{(\boldsymbol{t}\cdot\boldsymbol{e}_w)}{\cos\phi} & \frac{(\boldsymbol{b}\cdot\boldsymbol{e}_w)}{\cos\theta} \\ \frac{(\boldsymbol{t}\cdot\boldsymbol{e}_h)}{\cos\phi} & \frac{(\boldsymbol{b}\cdot\boldsymbol{e}_h)}{\cos\theta} \end{bmatrix} \boldsymbol{p} \leq \begin{bmatrix} W \\ H \end{bmatrix} \tag{44}$$

A. Computing feasible CoP solutions

The structure of Equation (42) suggests a particular solution: let us take $\boldsymbol{p}(s) = \boldsymbol{p}_i f(s\omega)$, where:

- $f(\omega_i) = 1$: initially, the CoP is located at $\boldsymbol{r}_i$;
- $f(0) = 0$: eventually, the CoP is located at $\boldsymbol{r}_f$;
- *f is increasing:* we exclude solutions where the CoP goes back and forth, that we deem suboptimal;
- *f is integrable:* let F denote its primitive such that $F(0) = 0$. It is positive by monotonicity of f.

With this choice, the boundedness condition (42) becomes

$$\boldsymbol{p}_i = \frac{\dot{\bar{\boldsymbol{c}}}_i + \omega_i \bar{\boldsymbol{c}}_i}{F(\omega_i)} \tag{45}$$

By monotonicity of f, the CoP trajectory is feasible if and only if its initial position $\boldsymbol{p}_i$ satisfies the feasibility condition (43). Considering (45), this can be written:

$$\boldsymbol{b}F(\omega_i) - (\mathbf{A}\bar{\boldsymbol{c}}_i)\omega_i \geq \mathbf{A}\dot{\bar{\boldsymbol{c}}}_i \tag{46}$$

We see here the general principle at work: in 2D, the strict constraint $\boldsymbol{p} = 0$ imposed a single value for ω_i; in 3D, the relaxed polygonal constraint $\mathbf{A}\boldsymbol{p} \leq \boldsymbol{b}$ frees a range of possible choices for ω_i. By increasing the number of potential solutions this will also ease the task of the convex optimizer.

At this stage, the roboticist can explore different CoP strategies via the choice of a (preferably convex) function F. Let us focus on the example of a power law where, for some $k \geq 1$:

$$f(s\omega) = \left(s\frac{\omega}{\omega_i}\right)^{k-1} \Longrightarrow F(\omega_i) = \frac{\omega_i}{k} \tag{49}$$

Equation (46) simplifies to:

$$\left(\frac{\boldsymbol{b}}{k} - \mathbf{A}\bar{\boldsymbol{c}}_i\right)\omega_i \geq \mathbf{A}\dot{\bar{\boldsymbol{c}}}_i \tag{50}$$

Each line of this vector inequality provides a lower or upper bound on ω_i, depending on the sign of the factor in front of it. Inequalities can thus be summed up in linear time as $\omega_{i,\min} \leq \omega_i \leq \omega_{i,\max}$. Note that this computation is only carried out once from the initial state, *i.e.* it is not part of the following optimization.

By definition of Φ, ω_i is equal to $\sqrt{\Phi_N}$, so that bounds on ω are mapped directly into the convex optimization as $\omega_{i,\min}^2 \leq \Phi_N \leq \omega_{i,\max}^2$. However, previously ω_i also appeared in the right-hand side of the convex equality constraint (38). In 3D, this constraint becomes:

$$\sum_{j=0}^{N-1} \frac{\Delta_j}{\sqrt{\Phi_{j+1}}+\sqrt{\Phi_j}} - \frac{\bar{z}_i}{g}\sqrt{\Phi_N} = \frac{\dot{\bar{z}}_i}{g} \tag{51}$$

Fortunately, $x \mapsto -\sqrt{x}$ is a convex function. The sum of two convex functions being convex, this new equality is again convex. Wrapping up these developments, we obtain Convex Program 2.

B. Model predictive control for 3D balance

Our pipeline for 3D balance is the same as in Section III. Once the optimal solution $\Phi_1^*, \ldots, \Phi_N^*$ of Convex Problem 2 is found, leg stiffness and CoP location are extracted as:

$$\omega_i^* = \sqrt{\Phi_N^*} \quad \lambda_i^* = \frac{\Phi_N^* - \Phi_{N-1}^*}{\Delta_{N-1}} \quad \boldsymbol{p}_i^* = \frac{\dot{\bar{\boldsymbol{c}}}_i + \bar{\boldsymbol{c}}_i \omega_i^*}{F(\omega_i^*)} \tag{52}$$

In the case of the power law (49), the CoP solution becomes:

$$\boldsymbol{p}^* = k \left[\boldsymbol{p}_i + \frac{\dot{\boldsymbol{p}}_i}{\omega_i^*} \right] \tag{53}$$

Interestingly, we recognize here the expression of the capture-point feedback control law [3], [5], under the same requirement $k \geq 1$, even though we are in the context of 3D balance where λ and ω are time-varying.

Convex Problem 2 is solved at basically the same speed as its 2D counterpart, on the scale of 1–3 ms with the setting described in Section V, but it is able to cope with both sagittal and lateral linear momentum. Its solutions tend to be flatter, which can be explained by the relaxed constraint (48) compared to (39): with only one end fixed and a wider set of choices for ω_i, it is easier to find solutions where λ varies less (favored by the quadratic cost function). By trying to keep λ constant as best as possible, Convex Problem 2 thus generates a hierarchical strategy: CoP variations are used first; then, if need be, CoM height variations are resorted to. This behavior is depicted in Figure 2.

C. Discussion: how did the problem become convex?

CoM trajectory generation using general 6D contacts is a notoriously nonconvex problem due to angular momentum. Even when a linear model is used and the angular momentum is regulated to zero [5], nonconvexity lingers in feasibility inequality constraints [13]. Nonconvex optimization provide one way to attack the problem using *e.g.* direct multiple shooting [14], however our experience in [15] met with a high solver failure rate that required dedicated countermeasures. Ponton *et al.* [16] proposed a convex relaxation of momentum dynamics by bounding the convex and concave parts of the angular momentum. Yet, in the present work we solve convex problems with no approximation of system dynamics nor feasibility constraints. Where is the difference?

Convexity is a property of the boundedness condition (22) over ω. The design choice here that extends this convexity to 3D balance is to make the CoP trajectory a *consequence* $\boldsymbol{p}(s) = \boldsymbol{p}_i f(s\omega)$ of ω, as opposed to *e.g.* a shooting method where $\boldsymbol{p}$ and ω would be optimized jointly. It also means that the choice of a CoP strategy encoded by $f(s\omega)$ has an impact on the existence of feasible solutions. This may happen for instance in example (49)–(53) when the feedback gain k is too large—which is by the way true for all capture-point based feedback controllers [3], [4], [5], [10], [17].

V. Stepping experiments

We implemented both balance controllers[1] and evaluated them in *pymanoid*[2], an extension of OpenRAVE for humanoid robotics. Convex problems were solved using the IPOPT solver,[3] with Jacobians and Hessians computed by automatic differentiation with CasADi.[4] Note that IPOPT is a general-purpose nonlinear solver designed for large-scale problems, while the problems at hand are both small and convex. Better performance may be achieved by more specialized solvers.

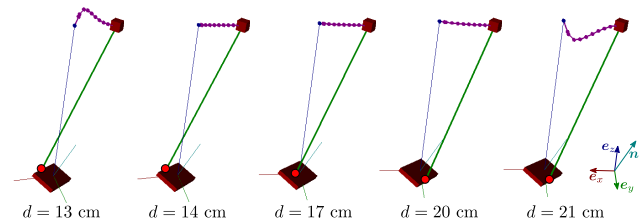

Fig. 2. **Saturation behavior of the 3D balance controller.** The horizontal distance from CoM to contact is denoted by d, $\boldsymbol{n}$ is the contact normal and red discs indicate the initial CoP. The controller keeps the CoM trajectory as close as possible to a LIPM via CoP variations. When this is not enough, height variations are resorted to for additional braking.

To assess the performance of solving Convex Problems 1 and 2, we run a benchmark over randomized contact locations and initial momenta. Both solvers were fed the same initial states, and sampling was biased toward viable states using the proxy distribution $z_{\text{crit}} \sim \frac{1}{2} z_f + \sigma_z \mathcal{U}([0,1])$. On an Intel Core i7-6500U CPU @ 2.50 Ghz, the computation times were almost identical: 1.8 ± 0.7 ms and 1.7 ± 0.6 ms for the 2D and 3D problem, respectively (averages and standard deviations over 10000 control cycles aggregated over 225 launches from different initial states).

We then evaluated 3D balance control on a push recovery scenario, using the CoP strategy (49) with $k = 2$. The setting, provided by Airbus Group, takes place in a 3D model of an A350 aircraft under construction. Due to *e.g.* an unexpected collision, or slippage over a ground obstacle that is only detected after momentum has built up, our model of the HRP-4 humanoid robot is imparted with an initial velocity of 1.4 $\mathrm{m\,s^{-1}}$. Note that, in this setting, preparing for hand contacts with the wall would be equally important, but we choose to focus here on the stance leg trajectory. A foothold is chosen on the fuselage as the kinematically reachable location with the lowest tilting. The velocity in the resulting frame (Figure 1) consists of roughly 1.3 $\mathrm{m\,s^{-1}}$ in the desired direction of motion $\boldsymbol{e}_x$, 0.2 $\mathrm{m\,s^{-1}}$ in the lateral direction $\boldsymbol{e}_y$ and 0.5 $\mathrm{m\,s^{-1}}$ along the vertical $\boldsymbol{e}_z$. We confirmed that the robot was able to stop in 1.5 s using a toe-to-heel CoP motion and a 10 cm CoM height variation. The scenario is depicted in Figure 3 and in the accompanying video.

VI. Concluding note

We saw how boundedness conditions provide a theoretical ground for convex model-predictive control of the center of mass in 3D. Future works towards a full-fledged walking controller will need to address questions such as contact switches and heel-to-toe CoP strategies.

[1] https://github.com/stephane-caron/3d-balance
[2] https://github.com/stephane-caron/pymanoid
[3] https://projects.coin-or.org/Ipopt
[4] http://casadi.org

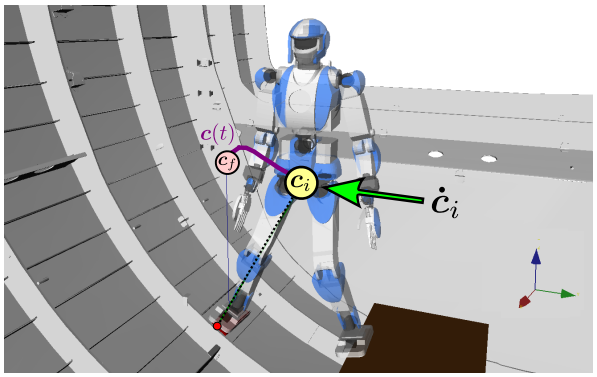

Fig. 3. **3D balance control using both CoP and CoM height variations.** The robot recovers from an undesired lateral push by stepping onto the fuselage of an A350 aircraft under construction. An initial velocity of 1.4 $\mathrm{m\,s^{-1}}$ is absorbed in 1.5 $\mathrm{m\,s^{-1}}$ using both the ankle strategy and a 10 cm CoM height variation.

References

[1] S. Kajita, F. Kanehiro, K. Kaneko, K. Yokoi, and H. Hirukawa, "The 3d linear inverted pendulum mode: A simple modeling for a biped walking pattern generation," in *Intelligent Robots and Systems, IEEE/RSJ International Conference on*, vol. 1, 2001, pp. 239–246.

[2] J. Pratt, J. Carff, S. Drakunov, and A. Goswami, "Capture point: A step toward humanoid push recovery," in *Humanoid Robots, IEEE-RAS International Conference on*, 2006, pp. 200–207.

[3] T. Sugihara, "Standing stabilizability and stepping maneuver in planar bipedalism based on the best com-zmp regulator," in *Robotics and Automation, IEEE International Conference on*, 2009, pp. 1966–1971.

[4] M. Morisawa, S. Kajita, F. Kanehiro, K. Kaneko, K. Miura, and K. Yokoi, "Balance control based on capture point error compensation for biped walking on uneven terrain," in *Humanoid Robots, IEEE-RAS International Conference on*, 2012, pp. 734–740.

[5] J. Englsberger, C. Ott, and A. Albu-Schäffer, "Three-dimensional bipedal walking control based on divergent component of motion," *IEEE Transactions on Robotics*, vol. 31, no. 2, pp. 355–368, 2015.

[6] O. E. Ramos and K. Hauser, "Generalizations of the capture point to nonlinear center of mass paths and uneven terrain," in *Humanoid Robots, IEEE-RAS International Conference on*, 2015, pp. 851–858.

[7] T. Koolen, M. Posa, and R. Tedrake, "Balance control using center of mass height variation: Limitations imposed by unilateral contact," in *Humanoid Robots, IEEE-RAS International Conference on*, 2016.

[8] W. Gao, Z. Jia, and C. Fu, "Increase the feasible step region of biped robots through active vertical flexion and extension motions," *Robotica*, vol. 35, no. 7, pp. 1541–1561, 2017.

[9] J. E. Pratt and S. V. Drakunov, "Derivation and application of a conserved orbital energy for the inverted pendulum bipedal walking model," in *Robotics and Automation, IEEE International Conference on*, 2007, pp. 4653–4660.

[10] M. A. Hopkins, D. W. Hong, and A. Leonessa, "Humanoid locomotion on uneven terrain using the time-varying divergent component of motion," in *Humanoid Robots, IEEE-RAS International Conference on*, 2014, pp. 266–272.

[11] L. Lanari, S. Hutchinson, and L. Marchionni, "Boundedness issues in planning of locomotion trajectories for biped robots," in *Humanoid Robots, IEEE-RAS International Conference on*, 2014, pp. 951–958.

[12] P.-B. Wieber, R. Tedrake, and S. Kuindersma, "Modeling and control of legged robots," in *Springer Handbook of Robotics*. Springer, 2016, pp. 1203–1234.

[13] S. Caron and A. Kheddar, "Multi-contact walking pattern generation based on model preview control of 3d com accelerations," in *Humanoid Robots, IEEE-RAS International Conference on*, 2016.

[14] J. Carpentier, S. Tonneau, M. Naveau, O. Stasse, and N. Mansard, "A versatile and efficient pattern generator for generalized legged locomotion," in *Robotics and Automation (ICRA), IEEE International Conference on*, 2016, pp. 3555–3561.

[15] S. Caron and A. Kheddar, "Dynamic walking over rough terrains by nonlinear predictive control of the floating-base inverted pendulum," in *Intelligent Robots and Systems, IEEE/RSJ International Conference on*, 2017.

[16] B. Ponton, A. Herzog, S. Schaal, and L. Righetti, "A convex model of humanoid momentum dynamics for multi-contact motion generation," in *Humanoid Robots, IEEE-RAS International Conference on*, 2016, pp. 842–849.

[17] A. Pajon, S. Caron, G. De Magistris, S. Miossec, and A. Kheddar, "Walking on Gravel with Soft Soles using Linear Inverted Pendulum Tracking and Reaction Force Distribution," in *Humanoid Robots, IEEE-RAS International Conference on*, 2017.

Appendix

A. Convexity of Equation (35)

Let us first consider the function $g(x,y) = \frac{1}{\sqrt{x}+\sqrt{y}}$. The trace and determinant of its Hessian $\nabla^2 g$ are:[5]

$$\mathrm{tr}(\nabla^2 g) = \frac{x^2 + 3(x+y)\sqrt{xy} + y^2}{4(xy)^{3/2}(\sqrt{x}+\sqrt{y})^3} \tag{54}$$

$$\det(\nabla^2 g) = \frac{3}{16(xy)^{3/2}(\sqrt{x}+\sqrt{y})^4} \tag{55}$$

Both are strictly positive quantities over the domain $x, y > 0$, therefore $\nabla^2 g$ is positive definite and f is convex.

Consider now the function $G(\mathbf{\Phi})$ defined by Equation (35) over the vector $\mathbf{\Phi}$ of positive values $\Phi_1, \ldots, \Phi_N$:

$$G(\mathbf{\Phi}) = \sum_{j=0}^{N-1} \Delta_j g(\Phi_{j+1}, \Phi_j) \tag{56}$$

Then, for any $t \in [0,1]$, we have by convexity of f:

$$G(t\mathbf{\Phi} + (1-t)\mathbf{\Phi}') \tag{57}$$

$$= \sum_{j=0}^{N-1} \Delta_j g(t\Phi_{j+1} + (1-t)\Phi'_{j+1}, t\Phi_j + (1-t)\Phi'_j)$$

$$\leq \sum_{j=0}^{N-1} \Delta_j \left[t g(\Phi_{j+1}, \Phi_j) + (1-t) g(\Phi'_{j+1}, \Phi'_j) \right] \tag{58}$$

$$= tG(\mathbf{\Phi}) + (1-t)G(\mathbf{\Phi}') \tag{59}$$

Which establishes that G is convex. ■

B. Computing time trajectories

The piecewise constant values of $\lambda(s)$ are directly given by $\lambda_j = (\Phi_{j+1} - \Phi_j)/\Delta_j$. Computing the time trajectory $\lambda(t)$ is then equivalent to finding the switch times t_j such that $s(t_j) = s_j$. Solving the equation of motion (1) of the IPM with constant λ, one can establish the recurrence relation:

$$t_j = t_{j+1} + \frac{1}{\sqrt{\lambda_j}} \log\left(\frac{\sqrt{\Phi_{j+1}} + \sqrt{\lambda_j} s_{j+1}}{\sqrt{\Phi_j} + \sqrt{\lambda_j} s_j} \right) \tag{60}$$

The same relation can be applied to find the map $s(t)$, giving $\omega(t) = \omega(s(t)) = [\Phi_i + \lambda_j(s(t)^2 - s_j^2)]^{1/2} s(t)^{-1}$ for $t \in [t_j, t_{j+1}]$ by Equation (31). Alternatively, one can solve the differential equation (3) from t_j to get directly:

$$\omega(t) = \sqrt{\lambda_j} \frac{1 - \upsilon_j \tanh(\sqrt{\lambda_j}(t - t_j))}{\upsilon_j - \tanh(\sqrt{\lambda_j}(t - t_j))} \tag{61}$$

where $\upsilon_j = \lambda_j / \omega(s_j) = \lambda_j s_j / \Phi_j$.

[5] To avoid painstaking calculations such as this one, we recommend using the online computational-knowledge engine Wolfram|Alpha provided by Wolfram Research, Inc.: `https://www.wolframalpha.com/`